RESEARCH ARTICLE | JUNE 05 2023

Phase distribution in nanochannels of supercritical fluid with different fluid–wall interactions ⊘

Wang Yan (王艳) ⓘ ; Xu Jinliang (徐进良) ✉ ⓘ ; Dong Ming (董明) ⓘ ; Xie Jian (谢剑) ⓘ ;
Wang Qinghua (王庆华)

Check for updates

View Online   Export Citation   CrossMark

Physics of Fluids   Journal of Applied Physics

Special Topic: Physics of 3D Printing

Submit Today!

AIP Publishing

AIP Publishing

Phase distribution in nanochannels of supercritical fluid with different fluid–wall interactions

View Online   Export Citation   CrossMark

Yan Wang (王艳),[1] Jinliang Xu (徐进良),[1,2,3,a] Ming Dong (董明),[2,3] Jian Xie (谢剑),[1,2,3]
and Qinghua Wang (王庆华)[1]

AFFILIATIONS

[1]Beijing Huairou Laboratory, Beijing 101400, China
[2]Beijing Key Laboratory of Multiphase Flow and Heat Transfer for Low Grade Energy Utilization,
  North China Electric Power University, Beijing 102206, China
[3]Key Laboratory of Power Station Energy Transfer Conversion and System, North China Electric Power University,
  Ministry of Education, Beijing 102206, China

[a]Author to whom correspondence should be addressed: xjl@ncepu.edu.cn

ABSTRACT

Supercritical fluids (SFs) are classically regarded as single-phase fluids without bubbles or interfaces, but a recent study shows nanobubbles in SFs under unconfined conditions. The objective of this paper is to explore the phase distribution under confined conditions. Molecular dynamics simulations are performed for supercritical argon. Two walls containing the SF have equal fluid–wall interactions with equal and unequal wall temperatures. An external force is applied on the top wall to control the pressure at $1.5P_c$, in which P_c is the critical pressure. Periodic boundary conditions are applied on the four side surfaces of the simulation box. The study indicates that the bulk fluid density is not only dependent on pressure and temperature, but also on fluid–wall interactions, this result deviates from the classical theory, where density depends on only pressure and temperature. For strong fluid–wall interactions, three- or five-layer structures are found, including liquid-like (LL) layers on the walls and two-phase-like (TPL) and gas-like (GL) layers (depending on bulk density) in the channel core. For weak fluid–wall interactions, the phase distribution becomes GL on the wall, and TPL and LL (depending on bulk density) in the channel core, which is inverse to those of strong fluid–wall interactions. Correspondingly, the phase distributions for strong and weak fluid–wall interactions can be analogous to annular or Leidenfrost patterns at subcritical pressures, respectively. The density profile is symmetric against the channel centerline at equal wall temperatures, but symmetry-breaking may exist when applying different wall temperatures. This work provides a phase-distribution link between subcritical and supercritical pressures, which is useful for the design and analysis of SF systems.

I. INTRODUCTION

Supercritical fluids (SFs) have received significant attention since their discovery by Cagniard de la Tour in 1822.[1] With temperatures and pressures of approximately 700 K and 75 bars, respectively, the deepest 12 km of atmosphere of Venus is so hot and dense that it behaves like an SF.[2] The magma generation beneath Rishiri Volcano could have been induced by the influx of SFs.[3] In addition, SFs are also applied in food processing,[4] chemical and petrochemical industries,[5] and thermal-power conversion systems.[6,7]

Classically, SFs are treated as single-phase fluids without bubbles or interfaces.[8] However, the single-phase fluid assumption is questioned in academia. Inelastic x-ray scattering and molecular dynamics (MD) simulations have shown that some thermophysical quantities (e.g., specific heat) have maxima that define a line emanating from the

critical point, which is called the Widom line.[9,10] These studies revealed a sharp transition of upon crossing the Widom line, demonstrating that the supercritical region is divided into gas-like (GL) and liquid-like (LL) regions.[9,11,12] Many investigations used radial distribution functions, structural factors, and two-body excess entropy methods to quantify the inhomogeneous structure of SFs.[13–17] Banuti[18] developed the transition temperature from LL to GL fluids when crossing the Widom line. Maxim *et al.*[19,20] monitored density fluctuations of supercritical water while the system evolved rapidly from LL to GL when crossing the Widom line during isobaric heating. Ha *et al.*[21,22] reported the classification of LL and GL molecules coexisting in the SF, identified by machine learning analysis on simulation data. Xu *et al.* investigated phase distribution of SFs under unconfined conditions.[23] In a regime map with pressure and temperature as the two

coordinates, three regimes can be categorized as LL, two-phase-like (TPL) and GL. In particular, the TPL regime occurs in a narrow temperature range across the pseudo-critical temperature, in which nanovoids are observed. Particles are sparsely distributed and have gas density inside the void but are densely populated and have liquid density outside the void. Voids have a curved interface, which is like bubbles at subcritical pressure. Thus, voids in the supercritical state are described as "bubblelike."[23] It is shown that the TPL regime consists of a mixture of bubble-like voids and surrounding liquids.

The above studies were performed under unconfined conditions for SFs. According to predictions from the United States Energy Information Administration, the production of shale gas can reach dozens of trillions of cubic feet in the next 20 years.[24] Carbon dioxide (CO_2) requires less pumping power and is used as fracturing and circulating fluid in hot dry rock geothermal energy extraction.[2,3,25,26] Moreover, the transport phenomena at the nanoscale have attracted attention in the fields of electronics, optics, and biologies.[27] Many studies can now be found on fluid flow and heat transfer in nanochannels at subcritical pressures.[28–30] The research progress of SFs in nanochannels is described as follows.

Adsorption of SFs in confined spaces: Heier *et al.*[31] studied the Lennard–Jones (LJ) fluid in a temperature range of $0.7T_c$, $0.77T_c$, $0.8T_c$, $0.9T_c$, $1.1T_c$, $1.5T_c$, and $2.0T_c$, where T_c is the temperature at the critical point and showed that the contact angle (CA) between the fluid and solid determines the adsorption strength. Li *et al.*[32] investigated the adsorption density, adsorption pressure, and adsorption enthalpy of a supercritical LJ fluid confined in slit-like pores. They found that if the wall–fluid potential was attractive, the adsorption density was greater than that of the bulk fluid, and that SF can undergo a "vapor-liquid phase transition" in attractive confined spaces. Guo *et al.*[33] investigated the adsorption behavior of supercritical methane in nanopores and found that the amount of methane adsorption decreases with increasing temperature and water content. Wang *et al.*[34] studied the adsorption behavior of supercritical methane in shale nanopores composed of different mineral types (organic matter, clay, and calcite) and found that water molecules in inorganic montmorillonite and calcite pores adsorb on the walls to form a water film, while water molecules in graphene organic pores aggregate in the center of the pores to form clusters.

Diffusion of SFs in confined spaces: Various MD simulations studies of SFs have focused on the diffusion of shale oil and gas. Wang *et al.*[34] showed that confined methane molecules diffused more rapidly with increased pore size and temperature but more slowly with increased pressure. Their findings provide a better understanding of hydrocarbon transport through shale formation. Cracknell *et al.*[35] found that self-diffusion decreases with concentration, and the dependence of transport diffusivity on concentration is determined by the pore size. Zhou *et al.*[36] investigated the diffusion of CO_2 confined in seven slit carbon pores (0.744–3.72 nm) from subcritical to supercritical pressures. Their results showed that the diffusion coefficients of CO_2 molecules confined in a slit pore under supercritical conditions were dependent on the fluid density in the pore, and the diffusion coefficients at supercritical temperatures were 5–15 times larger than those at subcritical temperatures. Gordillo *et al.*[37] studied water inside a carbon-slit pore at supercritical conditions, where the residence time of water at interfaces was like that in the central regions of the slabs, and water diffusion was much faster at low densities. Shan *et al.*[38]

found that small pore sizes and intense intermolecular interactions among gas–gas and gas–solid particles led to complex gas transport in shale nanopores. The overall mass flux was dominated by slip flow in bulk regions and enhanced surface diffusion in adsorbed regions in organic pores, but in inorganic pores, slip was not observed.[38]

Flow of SFs in confined spaces: Tuan *et al.*[39] demonstrated that at nanoscale, the flow of water with a hydrophilic surface was enhanced by a thin layer of supercritical carbon dioxide (sCO_2) at the water-solid interfaces. The sCO_2 functioned as an atomistic lubricant to transform a hydrophilic interface into a superhydrophobic one, triggering a boundary condition switch from stick to slip. Zhan *et al.*[40] and Shan *et al.*[38] studied the effect of wall surface type on the flow behavior of supercritical methane and found that the fluid velocity in organic graphene nanopores showed a plug-like flow distribution, while the velocity distribution in inorganic nanopores followed a parabolic pattern. Organic nanopores greatly increased velocity slip and improved oil and gas transport efficiency. Wang *et al.*[25] investigated the slip length of supercritical carbon dioxide and found that it gradually decreases with increasing temperature and pore size. Rough surface structures can reduce slip velocity and are related to pore size.

In summary, the research focusing on SFs in confined nanochannels is summarized as follows: (1) The adsorption of SFs in confined spaces is strongly dependent on fluid–wall-interactions. The adsorption behavior is enhanced near the wall for strong fluid–wall interactions.[31–34] (2) Diffusion of SFs in confined spaces becomes more prominent at supercritical pressures than at subcritical pressures. The pressures, pore sizes, and temperatures have a complicated influence on the diffusion of SFs.[34–38] (3) Boundary conditions at the wall can be changed from stick to slip for SFs in nanochannels, depending on the fluid and fluid–wall interaction intensities and other factors.[39–41]

The objective of this paper is to present an investigation of phase distribution in nanochannels and the effect of fluid–wall interaction (surface wettability) and wall temperature. Such a problem is important because the phase distribution strongly influences flow resistance and heat transfer at supercritical pressures. For example, at subcritical pressures, superhydrophobic surfaces create the Lotus leaf effect to yield ultra-small flow resistance for fluid transportation.[41] Additionally, high wall temperature may cause the Leidenfrost condition to deteriorate heat transfer between the surface and the fluid.[42] On the contrary, hydrophilic surfaces attach a thin liquid film on the wall to hold the annular flow or slug flow.[43] The liquid film thickness dominates the heat transfer behavior.[44] However, all these effects are unknown at supercritical pressures.

This paper shows the phase distribution in a SF with confined wall conditions using MD simulations. The structure of the paper is arranged as follows. Section II provides the details of the MD simulations. Section III reports the results and discussion, including four subsections. Section III A compares the system sizes between the confined and unconfined systems at equal pressures and bulk temperatures, emphasizing that the system size is changed for the confined system owing to the interactions between fluid and wall. It is further shown that the fluid density is not only dependent on the pressure and temperature but also on the fluid–wall interaction intensities. Sections III B and III C report the phase distributions under conditions of high, moderate, and low bulk densities of fluids with different fluid–wall interaction intensities. By comparing the cases of equal and unequal wall temperatures for the two walls confining the fluid, one can

identify how the phase distribution is influenced by the wall wettability and temperature. Comments are made in Sec. III D on the differences in phase distribution between subcritical and supercritical pressures.

II. MOLECULAR DYNAMICS SIMULATION

Figure 1 shows the physical model studied in this paper. The system contains a top and bottom solid wall; the former can move freely in the z direction to control the system pressure, but the latter is stationary at the macroscopic level. Argon fluid is contained between the two solid walls. Periodic boundary conditions are applied along the x and y directions. The system size is $L_x = L_y = 30\sigma$, where σ is the characteristic length of an argon atom, and the size in the z direction depends on the number of argon atoms and the running pressure of the fluid. The solid walls are composed of platinum (Pt), with a density of 21.45 g/cm^3. Each of the solid walls has eight layers. Initially, all the solid atoms are organized in the face-centered-cubic (fcc) structure. For each wall, the four layers of Pt atoms close to the fluid can oscillate freely, the next two layers act as a thermostat to maintain a constant wall temperature, and the outermost two layers are stationary to "freeze" the solid wall. Thus, during the computation, only the outermost two layers of solid atoms maintain the fcc structure, whereas other solid atoms deviate from the fcc structure. For each argon atom, the Newton equation is written as[45]

$$m_i \frac{d^2 \boldsymbol{r}_i}{dt^2} = \sum_{j \neq i, j=1}^{N} \boldsymbol{F}_{ij} + \sum_{j_s \neq i, j=1}^{N_s} \boldsymbol{F}_{ij_s}, \tag{1}$$

where m is the mass of an argon atom, $m = 6.69 \times 10^{-23}$ g, r is the distance between argon atom i and argon atom j or solid atom j_s, $\boldsymbol{F}_{ij}$ is the force between two argon atoms, $\boldsymbol{F}_{ij_s}$ is the force between argon atom i and solid atom j_s, i is the ith particle, and N and N_s are the total number of argon atoms and solid atoms involved in the system, respectively.

The force in Eq. (1) is expressed as $\boldsymbol{F} = \frac{\partial \phi(r)}{\partial \boldsymbol{r}}$, where ϕ is the potential energy between a pair of molecules such as argon atom i and argon atom j, or argon atom i and solid atom j_s. In this study, the LJ potential function is used for pair interactions between liquid–liquid atoms and solid–solid atoms,[46] such that
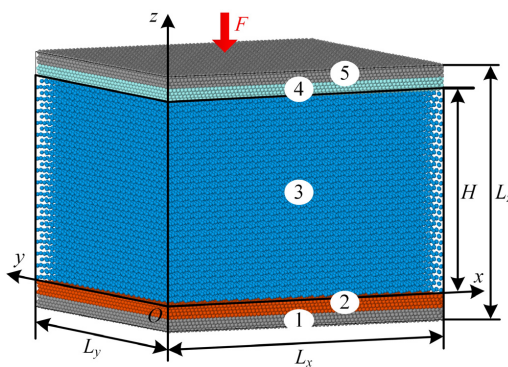

FIG. 1. Physical model studied in this paper. 1—fixed solid wall atoms, 2—solid layer that controls the temperature, 3—supercritical fluid (SF), 4—solid layer that controls the temperature, 5—solid wall that can move in z direction, F is the external force to control the system pressure.

$$\phi(r) = 4\varepsilon \left(\left[\frac{\sigma}{r} \right]^{12} - \left[\frac{\sigma}{r} \right]^{6} \right). \tag{2}$$

Equation (2) was initially developed by Lennard–Jones in 1931,[47] and the function is known as LJ potential. In Eq. (2), $\sigma_f = 0.3405$ nm, and ε_f is the energy scale of an argon atom ($\varepsilon_f = 1.67 \times 10^{-21}$ J). The equation is also used for pair interactions between solid atoms, with $\sigma_s = 0.2475$ nm and $\varepsilon_s = 8.35 \times 10^{-20}$ J. The subscripts f and s represent fluid and solid, respectively.

For solid–fluid interactions, Eq. (2) is modified as[48]

$$\phi(r_{ij}) = 4\alpha \varepsilon_{sf} \left[\left(\frac{\sigma_{sf}}{r_{ij}} \right)^{12} - \beta \left(\frac{\sigma_{sf}}{r_{ij}} \right)^{6} \right], \tag{3}$$

where ε_{sf} is obtained based on the Lorentz–Berthelot combining rule,[49] $\varepsilon_{sf} = \sqrt{\varepsilon_s \cdot \varepsilon_f}$, and $\sigma_{sf} = 0.5(\sigma_s + \sigma_f)$. The parameters α and β are used to adjust the intensity of the fluid–wall interaction intensity. At subcritical pressures, α and β determine the CA for a fluid on a wall surface.[52] Reference 52 used an optimal $\alpha = 0.14$ to simulate surface wettability from superhydrophilicity to superhydrophobicity conditions using a continuously varied β. This treatment was like that used in Ref. 50. The treatment of using α and β to simulate fluid–wall interaction intensity at subcritical pressures in this paper.

The Velocity–Verlet algorithm was used to integrate and solve the Newtonian equation. Using the acceleration, the calculation formulas for the position $\boldsymbol{r}$ and velocity of a particle $\boldsymbol{v}(t + \Delta t)$ at time $t + \Delta t$ are

$$\boldsymbol{r}(t + \Delta t) = \boldsymbol{r}(t) + \boldsymbol{v}(t)\Delta t + \frac{1}{2}\boldsymbol{a}(t)\Delta t^2, \tag{4}$$

$$\boldsymbol{v}(t + \Delta t) = \boldsymbol{v}(t + \Delta t/2) + \frac{1}{2}\boldsymbol{a}(t + \Delta t)\Delta t, \tag{5}$$

where $\boldsymbol{a}$ is the acceleration, $\boldsymbol{a} = \frac{d^2 \boldsymbol{r}_i}{dt^2}$, Δt is the time step, which is $\Delta t = 0.001\tau$, and $\tau = \sqrt{m\sigma^2/\varepsilon} = 2.16 \times 10^{-12}$ s is the timescale.

After the computation evolves into the steady stage, parameters are averaged in the height direction, along which the fluid domain is segmented into n layers, with each layer having a thickness of $\Delta z = L_z/n$. Two parameters are paid great attention, the particle number density ρ_i, having the unit of 1/m^3, and the temperature T_i having the unit of K. In the ith bin,

$$\rho_i = \frac{1}{(J_{start} - J_{end} + 1)L_x L_y \Delta z} \sum_{j=J_{start}}^{J_{end}} N_i^j, \tag{6}$$

where J_{start} and J_{end} are the start and end time step of the statistics, respectively. For N_i^j, the subscript i refers to the ith bin in the height direction and the superscript j refers to the jth time step.

The T_i is summary of the kinetic energies in the ith bin during a time duration from J_{start} to J_{end},

$$T_i = \frac{\sigma^3}{(J_{start} - J_{end} + 1)L_x L_y \Delta z} \sum_{j=J_{start}}^{J_{end}} \sum_{ii=1}^{N_i} m_i (v_{ii,j}^a)^2, \tag{7}$$

where the subscript ii refers to the iith particle in the ith bin of the simulation box, the superscript a refers to the three coordinates x, y, and z.

In this study, dimensionless parameters are used to characterize the density and phase distributions in the channel, including the non-dimensional density $\rho\sigma^3$ and non-dimensional temperature k_BT/ε, where k_B is the Boltzmann constant. All figures are presented using the non-dimensional form.

In this paper, both an unconfined system without walls and a confined system with two solid walls are studied. Based on thermodynamics at supercritical pressures, fluid density (ρ) depends on fluid pressure (P) and temperature (T), that is, $\rho = f(P, T)$. For the unconfined system, if one fills a specific number of fluid molecules in a given volume of the system, the fluid density can be determined. The fluid pressure is also determined if one further specifies the fluid temperature. The pressure determined by the MD simulations is in good agreement with well matches the value cited from the NIST software. However, the problem is more complicated for the confined system when the two solid walls are involved. Under such circumstances, the fluid pressure is not only dependent on the number of particles and the system volume, but it is also influenced by the temperatures of the two walls and the fluid–wall interaction intensity. If the same number of particles are filled in the unconfined system and confined system, the fluid pressures are different for identical volume of the two systems. If one expects to obtain the same pressure in the two systems, the volumes may be different.

To compare the results at the same pressure in both the confined and unconfined systems, it is important to control the system size in the z direction for the confined system to maintain the same pressure. There are two methods to control the system pressure: the canonical ensemble (NVT) method and the constant-pressure-temperature ensemble (NPT) method. The NVT method refers to a type of ensemble in statistical mechanics that is characterized by a constant number of particles (N), constant volume (V), and constant temperature (T). The NPT method refers to a type of ensemble in statistical mechanics that is characterized by a constant number of particles (N), constant pressure (P), and constant temperature (T). These two methods are not suitable for the confined system because the pressure is influenced by the surface wettability and wall temperatures. The NVT ensemble was only used in the first stage of equilibration in this work. Hence, a mechanical pressure control method was used, which is realized by applying a force (F) on the piston wall.[51] Referring to Fig. 1, the following equations are applied:[51]

$$F = PA, \tag{8}$$
$$f = PA/n_p, \tag{9}$$

where A is the planar area of $A = L_xL_y$, f is the force applied to a single solid atom, P is the target pressure, which is set as $1.5P_c$ in this paper—where P_c is the critical pressure of the fluid—and n_p is the total number of solid atoms.

A. Calculation procedure

The MD simulations of the unconfined system involve periodic boundary conditions applied over all six planes. The treatment for such a problem is well documented in Ref. 23. In this paper, a SF in the confined system is characterized by two wall temperatures T_{hot} (bottom wall) and T_{cold} (top wall), and two fluid–wall-interaction intensities, represented by β_h for the bottom wall and β_c for the top wall, as listed in Table I.

The MD simulations in the confined channels have the following three steps:

TABLE I. The parameters for the simulation cases.

	Particle density at initial state ($\rho\sigma^3$)	Fluid temperature at initial state (K)	Hotter wall temperature (K)	Cold wall temperature (K)	Wall wettability ($\alpha = 0.14$)
					Hotter wall and colder wall
(a1) LL					
1	0.5137	152.2 ($k_BT/\varepsilon = 1.2583$)	167.2 ($k_BT/\varepsilon = 1.3823$)	137.2 ($k_BT/\varepsilon = 1.1343$)	$\beta = 0.9$ (8.7°)
2					$\beta = 0.7$ (38.6°)
3					$\beta = 0.5$ (91.3°)
4					$\beta = 0.2$ (160.8°)
(a2) TPL					
1	0.3696	160.9 ($k_BT/\varepsilon = 1.3302$)	175.9 ($k_BT/\varepsilon = 1.4542$)	145.9 ($k_BT/\varepsilon = 1.2062$)	$\beta = 0.9$ (8.7°)
2					$\beta = 0.7$ (38.6°)
3					$\beta = 0.5$ (91.3°)
4					$\beta = 0.2$ (160.8°)
(a3) GL					
1	0.1537	188.4 ($k_BT/\varepsilon = 1.5576$)	203.4 ($k_BT/\varepsilon = 1.6816$)	173.4 ($k_BT/\varepsilon = 1.4336$)	$\beta = 0.9$ (8.7°)
2					$\beta = 0.7$ (38.6°)
3					$\beta = 0.5$ (91.3°)
4					$\beta = 0.2$ (160.8°)

- Step 1: the top wall, the bottom wall, and the fluid are set at the same temperature of $0.5(T_{hot} + T_{cold})$. The NVT method is used to ensure that the whole system reaches equilibrium temperature.
- Step 2: the Langevin method[52] is used to control the top wall temperature (T_{cold}) and the bottom wall temperature (T_{hot}). The NVE (microcanonical ensemble) is applied for fluid particles. Meanwhile, an external force is applied on the top wall to achieve a system pressure of $1.5P_c$ and the system size (L_z) is determined accordingly.
- Step 3: Following steps 1 and 2, the system runs for an additional 2000 τ for parameter averaging. LAMMPS (Large-scale Atomic/Molecular Massively Parallel Simulator)[53] is used for the simulation, and the OVITO software is used for a snapshot analysis of the argon atoms. A set of bins are divided along the z direction. The fluid density in the ith bin (ρ_i) is defined as the number of particles (N_i) divided by the volume of the bin: $\rho_i = N_i/(A\Delta z)$, where A is the planar area and Δz is the bin thickness. Non-dimensional parameters are also used: $x* = \frac{x}{\sigma}$, $y* = \frac{y}{\sigma}$, $z* = \frac{z}{\sigma}$, and $t* = \frac{t}{\tau}$, where $\tau = \sqrt{m\sigma^2/\varepsilon} = 2.16 \times 10^{-12}$ s is the characteristic time of the argon fluid.

B. Molecule marking technique and phase distribution in the system

Because fluid particles are non-uniformly distributed in the system, it is necessary to mark each fluid particle as either a gas molecule

or a liquid molecule. The molecule marking technique was reported in Refs. 54 and 55 and is considering a sphere of radius 1.5σ encircling a target molecule and its neighboring molecules (marked as $j = 1, 2, \ldots n$), where n is the maximum number of molecules that can be included in the sphere excluding the target molecule. The target molecule is marked as a liquid molecule if $n \geq 5$, or as a gas molecule if $n < 5$.[59] The liquid and gas molecules are marked as blue and yellow, respectively [see Fig. 2(a)]. Xu et al.[23] defined vapor mass quality at supercritical pressure as $\chi_{gas} = N_{gas}/N$, where N_{gas} and N are the number of gas molecules and the total number of molecules in the system, respectively. In each system, an SF attain LL, TPL, and GL phases at $\chi_{gas} < 0.1$, $0.1 < \chi_{gas} < 0.9$, and $\chi_{gas} > 0.9$, respectively [see Fig. 2(a)].

A plot of $\rho\sigma^3$ vs T/T_c for argon at $1.5P_c$ is shown in Fig. 2(b), where ρ is the particle density, defined as the number of argon particles divided by the system volume; and T and T_c are the temperature and critical temperature, respectively. The three regimes of LL, TPL, and GL are marked in Fig. 2(b), in which the TPL regime contains a bubble-like structure. Two transition densities are marked: $\rho\sigma^3 = 0.4798$ for the transition from LL to TPL, and $\rho\sigma^3 = 0.1696$ for the transition from TPL to GL. In fact, at $1.5P_c$, these values are the minimum density for the LL regime and the maximum density for the GL regime, respectively. Point a_1 refers to $T/T_c = 1.01$ and $\rho\sigma^3 = 0.5137$ in the LL regime, point a_2 refers to $T/T_c = 1.068$ and $\rho\sigma^3 = 0.3696$ in the TPL regime, and point a_3 refers to $T/T_c = 1.25$ and $\rho\sigma^3 = 0.1537$ in the GL regime. We note that Figs. 2(a) and 2(b)
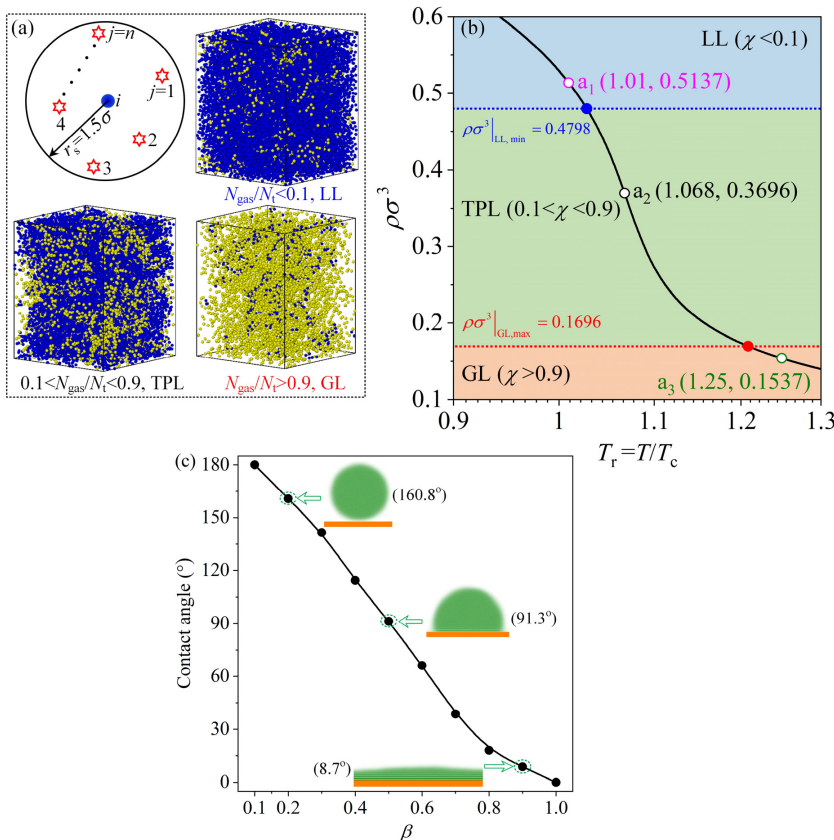

FIG. 2. The calculation cases in supercritical pressure and contact angle (CA) in subcritical pressure. (a) The atoms marking technique to identify each atom belongings to liquid atom or gas atom, the three snapshot pictures for unconfined system are at $2.5P_c$ and $1.0T_c$ for LL, $2.5P_c$ and $1.17T_c$ for TPL, $2.5P_c$ and $1.7T_c$ for GL, respectively. (b) Non-dimensional densities vs non-dimensional temperatures in unconfined system, in which points a_1, a_2 and a_3 are the three calculation cases conducted in this study. (c) Contact angle vs the parameter β in subcritical pressure, in which CA equals to $160.8°$, $91.3°$, and $8.7°$ at $\beta = 0.2$, 0.5, and 0.9, respectively. In (c), data are recalculated and the curve is replotted based on Ref. 42.

are obtained for the unconfined system, and the three cases of a_1, a_2, and a_3 are selected as reference cases to be compared with those in the confined system.

At subcritical pressures, the CA characterizes the surface wettability influenced by the fluid–wall interaction intensity.[44] To understand how the CA is influenced by α and β, an MD simulation was performed for an argon droplet on a wall surface, using $\alpha = 0.14$ and β values in the range 0.1–1.0. The simulation was performed at thermal equilibrium with a saturation temperature of 100 K. It is important to identify the location of the vapor–liquid interface, which is defined here as at $0.5(\rho_l + \rho_v)$, where ρ_l and ρ_v are the liquid density and the vapor density, respectively. Figure 2(c) shows that CA decreases as β increases from 0.1 to 1.0 while keeping $\alpha = 0.14$. Droplet topographies are presented for three cases: $CA = 160.8°$, $91.3°$, and $8.7°$. Figure 2(c) also shows increased fluid–wall-interaction when β increases. Figure 3 shows the flow diagram for the molecule marking technique and identification of phase distribution in nano-channels.

The present work applies the molecules marking technique to identify a fluid molecule belonging to the liquid state or gas state. Such a technique is widely used in previous articles. Ten Wolde and Frenkel[54] used the neighboring molecules method to determine the properties of particles to study the gas–liquid nucleation of the LJ fluid. For a target molecule, the neighboring molecules are encircled in a specified radius of $r_c = 1.5\sigma$ sphere.[54] They found that the probability distribution of liquid and gas is dependent on the number of

neighboring molecules at the coexistence point.[23,54] When the number of neighboring molecules is less than five, there is the largest probability for the target molecule being in a gas state. Alternatively, if the number of neighboring molecules is larger than five, the target molecule has the largest probability of being liquid state. Hence, the number of 5 is the dividing line.[23,54] Similarly, Wedekind and Reguera[56] labeled a molecule to be liquid when it has at least five neighbors during their study of vapor condensation. Losey and Sadus[55] extended the molecule marking method to SF.

III. RESULTS AND DISCUSSION

A. System size comparison between confined and unconfined systems

When the unconfined system is changed to the confined system, the fluid density is dependent on both the initial fluid state (LL, TPL, and GL) and the fluid–wall interaction intensity. Figure 4(a) shows a snapshot of the distribution of argon particles for reference case a_3 shown in Fig. 2(b) ($T = 1.25T_c$, $\rho\sigma3 = 0.1537$). The total number of argon atoms is 10 976 for the unconfined system with a volume of $30\sigma \times 30\sigma \times 36.5\sigma$. For the confined system, and keeping L_x and L_y identical to those of the unconfined system, the average particle density increases from 0.1537 to 0.1782 when the same number of particles fills the space between the two solid walls, with $\beta_h = 0.9$ and $k_B T_{hot}/\varepsilon = 1.6182$ for the hot wall (bottom wall), and $\beta_c = 0.9$ and $k_B T_{cold}/\varepsilon = 1.4336$ for the cold wall (top wall). We note that the average temperature of the two solid walls equals $k_B T_{ave}/\varepsilon = 1.5576$ for the unconfined system. Correspondingly, the height of the simulation box decreases from 36.5σ to 31.5σ [see Fig. 4(b)]. For strong fluid–wall interactions such as those encountered in Fig. 4(b), the wall attracts and adsorbs more fluid particles, increasing the average density in the confined system. This is true for sparsely distributed particles in the system. The relative deviations of the densities between the confined system and the unconfined system are summarized in Fig. 4(c). The results are presented in three groups, with $\beta_h = \beta_c = 0.9$, 0.5, and 0.2, respectively. For the confined system, the density is greater than that of the unconfined system only under the condition of strong fluid–wall interaction and an initial GL state (a_3 case), the other working conditions show that the density is lower than the unconfined system. Controlling the pressure is important for comparing the unconfined system with the confined system. Figure 4(d) shows the control outcomes for the non-dimensional pressures for the three groups of β values. The desired pressure is set as $1.5P_c$, demonstrating a maximum deviation of 5% between the real and desired pressure of the system.

The phase distribution in the nanochannels is influenced by the particle density ($\rho\sigma^3$) and the temperature and fluid–wall-interaction of the two walls. The particle density profiles in the channel height direction can be obtained. A local region is believed to be LL, TWL, and GL if its particle density is such that $\rho\sigma^3 > 0.4798$, $0.1696 < \rho\sigma^3 < 0.4798$, and $\rho\sigma^3 < 0.1696$, respectively. Thus, the phase distribution in the channel height direction can be identified. In Secs. III B–III–D, we first present the outcomes for the cases with unequal wall temperatures, followed by the cases with equal wall temperatures. The phase distributions are compared between supercritical pressures and subcritical pressures.
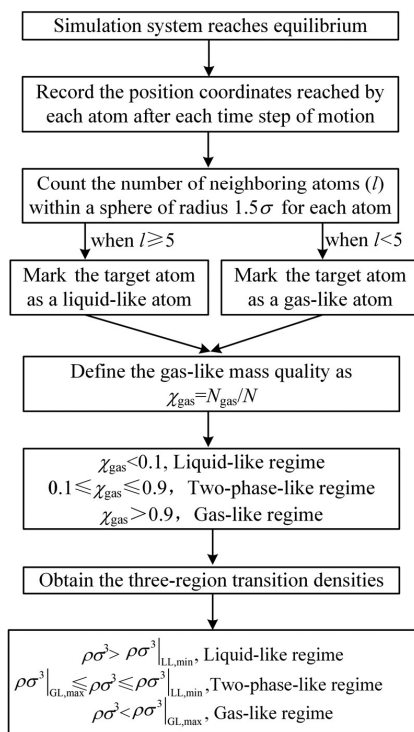

Flow diagram content:

- Simulation system reaches equilibrium
- Record the position coordinates reached by each atom after each time step of motion
- Count the number of neighboring atoms (l) within a sphere of radius 1.5σ for each atom
  - when $l \geq 5$: Mark the target atom as a liquid-like atom
  - when $l < 5$: Mark the target atom as a gas-like atom
- Define the gas-like mass quality as $\chi_{gas} = N_{gas}/N$
- $\chi_{gas} < 0.1$, Liquid-like regime
  $0.1 \leq \chi_{gas} \leq 0.9$, Two-phase-like regime
  $\chi_{gas} > 0.9$, Gas-like regime
- Obtain the three-region transition densities
- $\rho\sigma^3 > \rho\sigma^3|_{LL,min}$, Liquid-like regime
  $\rho\sigma^3|_{GL,max} \leq \rho\sigma^3 \leq \rho\sigma^3|_{LL,min}$, Two-phase-like regime
  $\rho\sigma^3 < \rho\sigma^3|_{GL,max}$, Gas-like regime

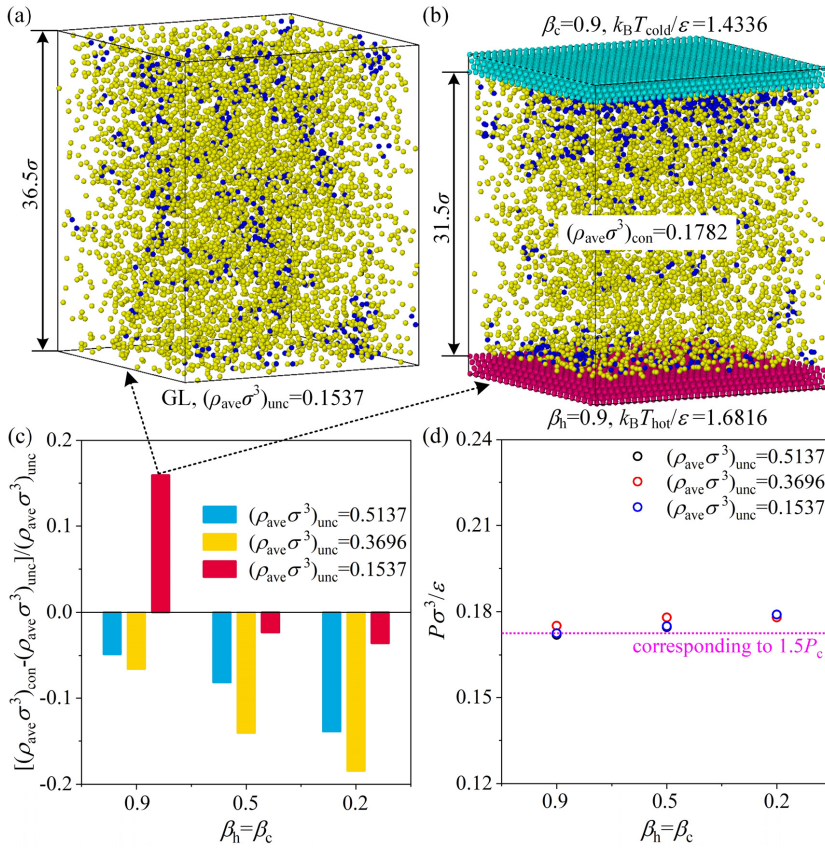**FIG. 3.** The flow diagram for molecules marking technique and identification of phase distribution.

FIG. 4. Average densities in unconfined system and confined system. (a) Snapshot picture for unconfined argon in GL regime with $\rho_{ave}\sigma^3 = 0.1537$. (b) snapshot picture for confined argon to keep the same pressure of $1.5P_c$. (c) The relative variation of densities for confined system with respect to unconfined system. (d) The outcomes by the controlling pressure technique in confined system with different fluid–wall interactions.

B. Phase distribution of SF in nanochannels with unequal wall temperatures

1. High-density case

The high-density case refers to a_1 in Fig. 2(b). Figures 5 and 6 show snapshots of the phase distributions and the density profiles in the channel height direction for strong fluid–wall-interaction [Fig. 5(a)], weak fluid–wall interaction [Fig. 5(b)], and moderate fluid–wall interaction (Fig. 6), respectively. Two transition lines, $\rho\sigma^3|_{GL,max}$ and $\rho\sigma^3|_{LL,min}$, are marked in Figs. 5 and 6. The local fluid is regarded as LL if $\rho\sigma^3 \geq \rho\sigma^3|_{LL,min}$ and GL if $\rho\sigma^3 \leq \rho\sigma^3|_{GL,max}$; otherwise, it is regarded as TPL with $\rho\sigma^3|_{GL,max} \leq \rho\sigma^3 \leq \rho\sigma^3|_{LL,min}$, where the TPL fluid is a mixture of LL and GL (nanobubbles) fluids. For the large-fluid–wall interaction case with $\beta_h = \beta_c = 0.9$ shown in Fig. 5(a), the density profile has a non-uniform distribution in the channel, showing the coupling effect of the fluid–wall-interaction and wall temperatures ($k_B T_{cold}/\varepsilon = 1.1343$ for the top wall and $k_B T_{hot}/\varepsilon = 1.3823$ for the bottom wall). Three regimes are identified: an LL layer with a thickness of 20.51σ near the cold wall covering half of the channel height, a TPL layer with a thickness of 16σ, and an LL layer with a thickness of 2.47σ close to the hot wall. The higher temperature of the bottom wall ensures that there is sufficient energy to separate the neighboring fluid particles, yielding the TPL layer adjacent to the very thin LL layer near the hot wall. Nanobubbles tend to populate near the hot wall under larger fluid–wall interaction conditions. On the contrary, LL molecules tend to populate near the cold wall.

The density profile assumes a uniform distribution under a weak fluid–wall interaction [see Fig. 5(b)]. Five layers are observed: two GL layers with a thickness of 2σ near the two walls, two symmetrically distributed TPL layers, and a center layer of LL covering 68% of the channel height. The effects of fluid–wall interaction and wall temperatures are decoupled under a weak fluid–wall interaction. By comparing Figs. 5(a) and 5(b), it is observed that a strong fluid–wall interaction creates a LL layer near the wall and a TPL layer (including bubbles) in the channel center, which can be analogized to annular flow at subcritical pressures.[43] The weak interaction between wall and fluid creates a vapor layer close to the wall, which is analogized to the Leidenfrost pattern at subcritical pressures.[42] Physically, there are two effects to locate the vapor phase near the wall at subcritical pressures: the repulsion-effect-induced vapor on the wall owing to the weak interaction between wall and fluid [e.g., Fig. 5(b)], and the high-wall-temperature-induced vapor on the wall, which is called the Leidenfrost effect. Figure 6 shows the phase distribution under moderate fluid–wall interaction intensity, which is like that in Fig. 5(a). By decreasing the interaction intensity from that shown in Fig. 5(a) to Fig. 6, the thickness of the LL layer increases, covering 73% of the channel height near the cold wall.

2. Low-density case

The low-density case refers to point a_3 ($\rho\sigma^3 = 0.1537$ with a pressure of $1.5P_c$ and a temperature of $1.25T_c$). Fluid particles are sparsely
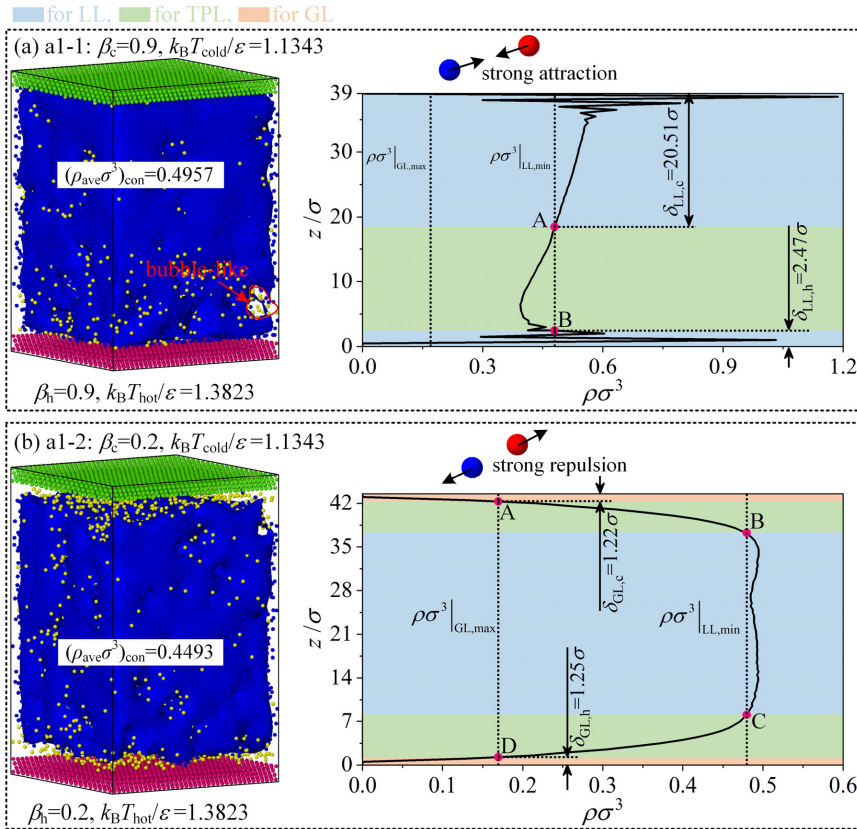
FIG. 5. Phase distribution with non-equal-wall-temperature and the initial sate of a_1. (a) Strong fluid–wall interaction with $\beta_h = \beta_c = 0.9$. (b) Weak fluid–wall interaction with $\beta_h = \beta_c = 0.2$.

populated and display GL properties in the unconfined system. Figures 7(a) and 7(b) show the phase distribution under strong and weak fluid–wall interactions, respectively. The top wall is colder ($k_B T_{cold}/\varepsilon = 1.4336$), and the bottom wall is warmer ($k_B T_{hot}/\varepsilon = 1.6182$). Owing to the fluid–wall interaction, the particle density is 0.1782 in Fig. 7(a) and 0.1482 in Fig. 7(b), deviating from 0.1537 for the unconfined system. Under a strong fluid–wall interaction, the particle density is highest on the cold wall, decreases sharply moving away from the cold wall, reaches a quasi-uniform distribution along the

channel height, and increases again near the hot wall, displaying weak symmetry-breaking. Correspondingly, the channel has five layers of fluid structures across the channel height, including two layers of LL near the hot wall and cold wall, two layers of TPL with nanobubbles away from the two walls, and a central populated GL region. The non-symmetrical distribution of densities is improved under a low particle density compared with a large particle density [see Fig. 5(a)], indicating that the phase distribution is dominated by the wall wettability and weakly influenced by the wall temperatures.
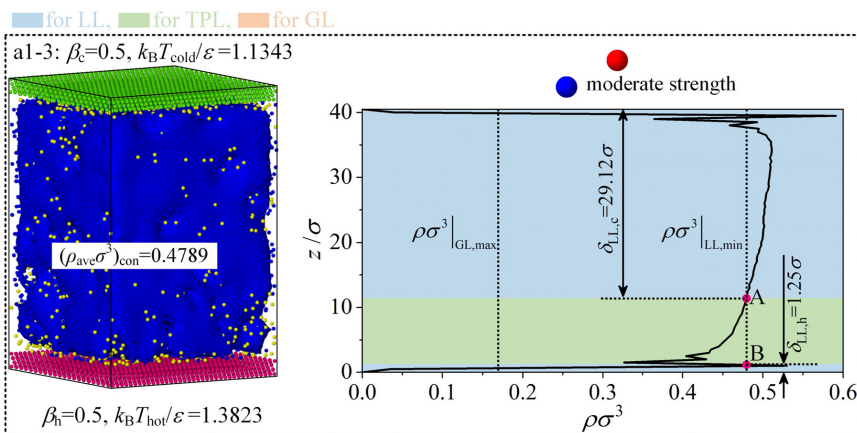

FIG. 6. Phase distribution with non-equal-wall-temperature and moderate fluid–wall interaction with $\beta_h = \beta_c = 0.5$ and the initial sate of a_1.
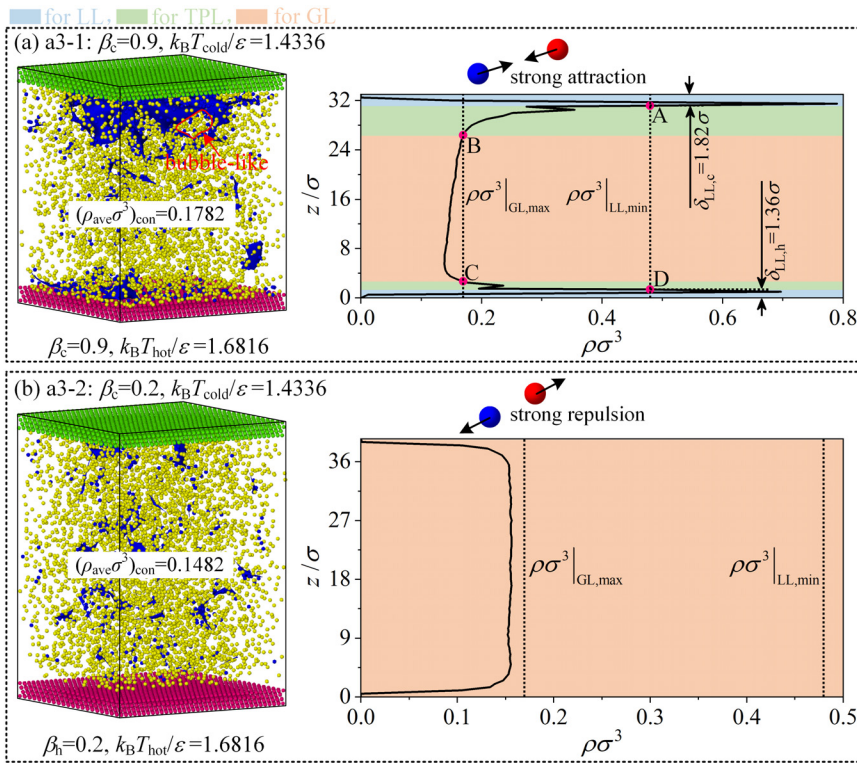
FIG. 7. Phase distribution with non-equal-wall-temperature and the initial sate of a_3. (a) Strong fluid–wall interaction with $\beta_h = \beta_c = 0.9$. (b) Weak fluid–wall interaction with $\beta_h = \beta_c = 0.2$.

As shown in Fig. 7(b), a weak fluid–wall interaction yields a uniform density distribution. The whole channel is occupied by GL, which is like the fluid structure in the unconfined system. The moderate fluid–wall interaction also creates a quasi-uniform density profile with GL fluid dominant in the channel except for a thin LL layer near the wall (see Fig. 8).

3. Moderate-density case

In Fig. 2(b), point a_2 belongs to the moderate-density case to maintain a TPL structure (with nano-bubbles) in the unconfined system. Here, we examine how wall wettability changes the phase distribution in the nanochannel. Again, we see that the density profile is strongly deformed, with a nonsymmetrical distribution in the channel under a strong fluid–wall interaction [see Fig. 9(a)], which is similar to that under large-density conditions [see Fig. 5(a)]. In contrast, a weak fluid–wall interaction yields a perfectly symmetrical density profile distribution, decoupling the combined effects of surface wettability and wall temperatures [see Fig. 9(b)]. A GL layer attaches to each wall, covering a thickness of a couple of molecular diameters. The bulk region of the channel is occupied by TPL, with nanobubbles distributed in the liquid. Because the overall density is not high, a pure LL structure is not observed, which is different from the high-density case shown in Fig. 5(b). Figure 10 shows the case for moderate fluid–wall
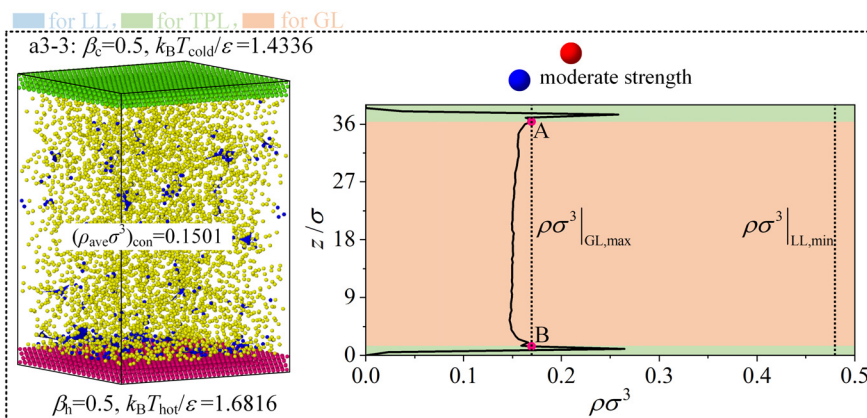

FIG. 8. Phase distribution with non-equal-wall-temperature and moderate fluid–wall interaction with $\beta_h = \beta_c = 0.5$ and the initial sate of a_3.
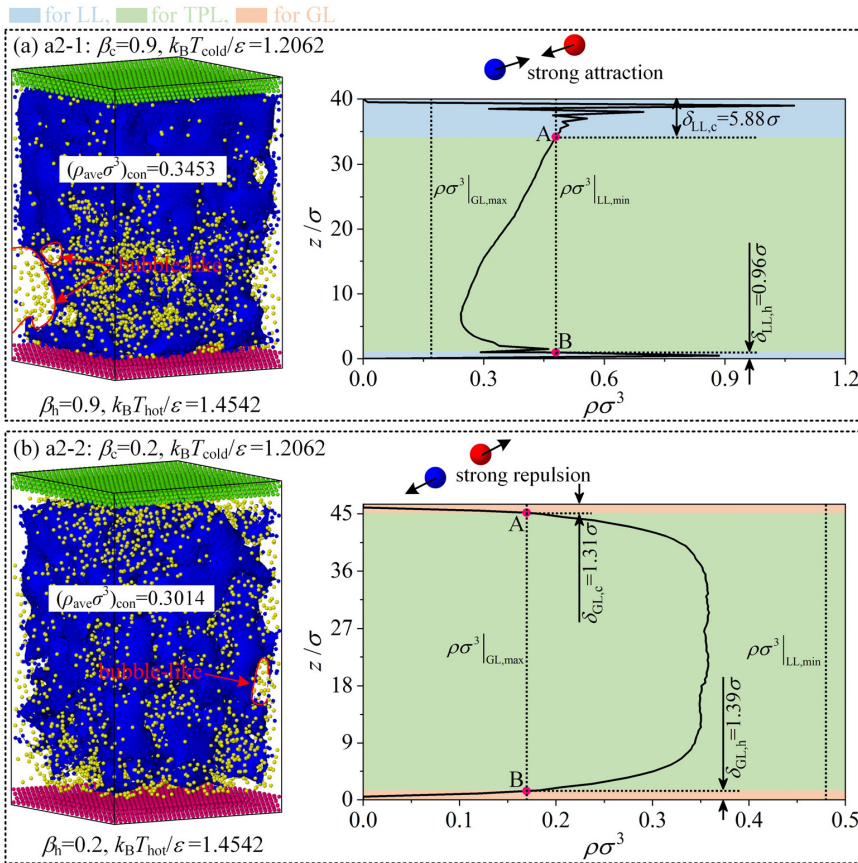
FIG. 9. Phase distribution with non-equal-wall-temperature and the initial sate of a$_2$. (a) Strong fluid–wall interaction with $\beta_h = \beta_c = 0.9$. (b) Weak fluid–wall interaction with $\beta_h = \beta_c = 0.2$.

interaction, where the whole channel is occupied by the TPL structure, without any LL or GL film attached to the wall. This case is like that of the unconfined system. However, the particle density is higher near the cold wall side and lower near the hot wall side, where a warmer wall temperature tends to increase the distance between fluid particles.

C. Phase distribution of SF in nanochannels with equal wall temperatures

The preceding discussion refers to unequal temperatures of the top wall and bottom wall. This section presents the equal-wall-temperature condition, as shown in Figs. 11 and 12. By comparing the unequal and equal wall temperatures cases, one can identify the
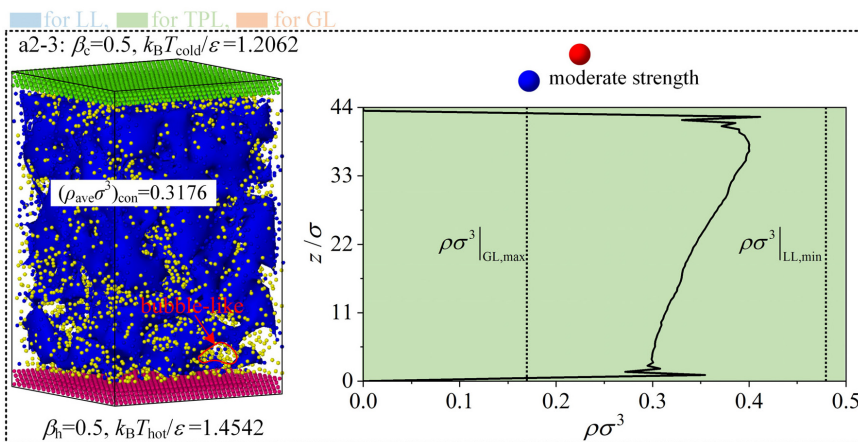

FIG. 10. Phase distribution with non-equal-wall-temperature and moderate fluid–wall interaction of $\beta_h = \beta_c = 0.5$ and the initial sate of a$_2$.
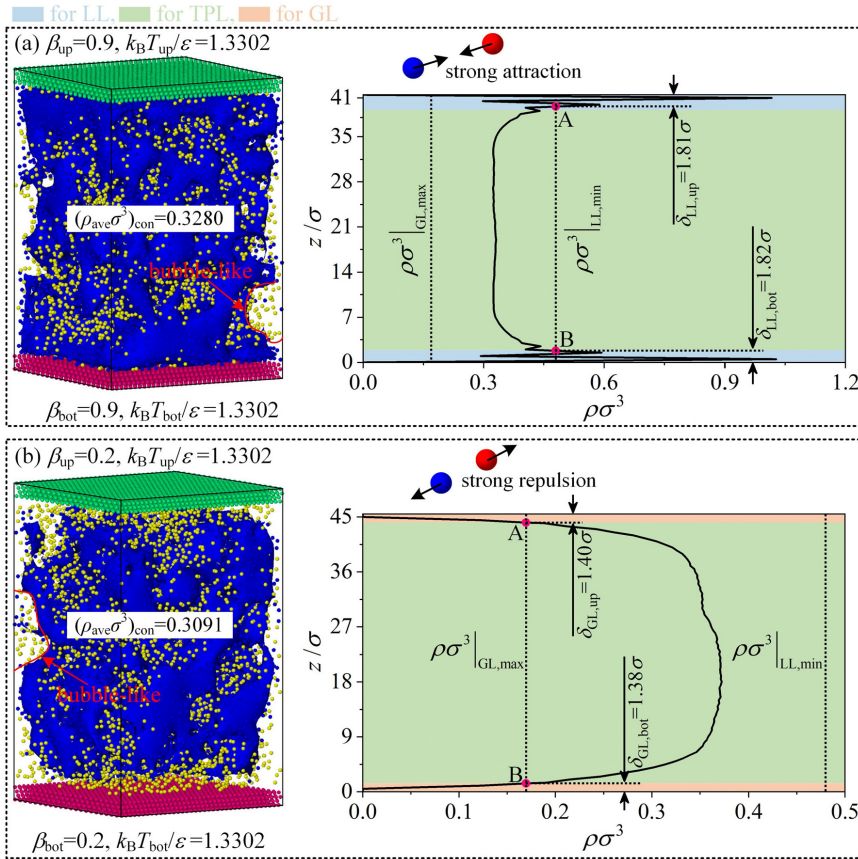
FIG. 11. Phase distribution with equal-wall-temperature and the initial sate of a_2. (a) Strong fluid–wall interaction with $\beta_h = \beta_c = 0.9$. (b) Weak fluid–wall interaction with $\beta_h = \beta_c = 0.2$.

separate effects of surface wettability and wall temperatures on the phase distribution. Figures 11(a), 11(b), and 12 show the phase distribution and density profiles in the nanochannel under strong, weak, and moderate fluid–wall interactions, respectively. The calculation conditions in Figs. 11 and 12 correspond to the moderate particle density case, referring to point a_2 in Fig. 2(a). It is seen that for equal wall temperatures, the density profile and phase distribution are symmetrically distributed against the channel centerline. Owing to the moderate-density case being used, the bulk region of the channel is occupied by TPL fluid containing nanobubbles. As shown in Fig. 11(a), the increased surface wettability maintains an LL layer with a thickness of ∼1.8σ on each of the two walls. In contrast, under a
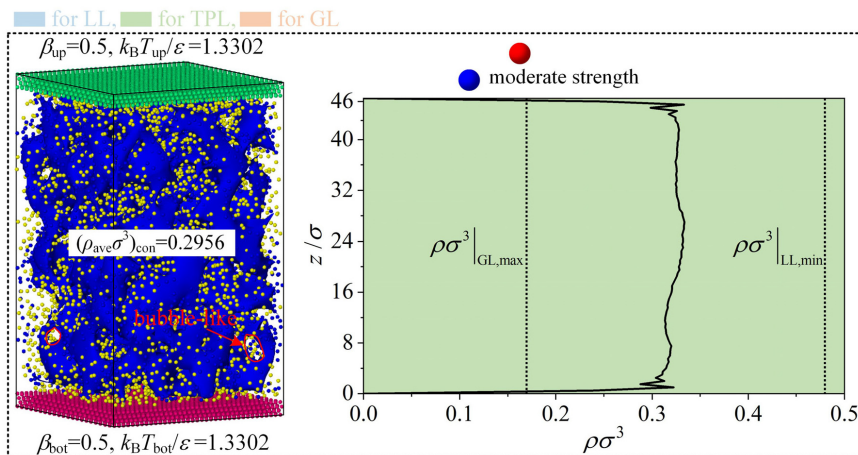

FIG. 12. Phase distribution with equal-wall-temperature and moderate fluid–wall interaction with $\beta_h = \beta_c = 0.5$ and the initial sate of a_2.

weak fluid–wall interaction, a GL layer with a thickness of $\sim 1.4\sigma$ is found on each of the two walls. Under a moderate fluid–wall interaction, the phase distribution and density profile are very uniform in the channel (see Fig. 12), approaching those in the unconfined system.

D. Analogy of phase distribution between supercritical pressure and subcritical pressure

At supercritical pressures, fluid density is dependent on fluid pressure and temperature. However, this work indicates that under confined conditions in nanoscale, fluid density is not only dependent on fluid pressure and temperature but also on wall wettability. The vapor mass quality χ_{gas} is defined as $\chi_{gas} = N_{gas}/N$, where N_{gas} is the number of vapor molecules and N is the total number of molecules in the system. We present χ_{gas} in Fig. 13(a) for the moderate-density case, referring to a_2 in Fig. 2(b). The fluid has a TPL structure with a χ_{gas} of ~ 0.25 for the unconfined condition. However, the fluid confinement ensures a larger χ_{gas} than that of the unconfined system, for both a weak fluid–wall interaction corresponding to a smaller β, and for a strong fluid–wall interaction corresponding to a larger β. The weak interaction induces a repulsion effect between fluid and wall that increases the distance between fluid particles, explaining the larger χ_{gas} in the confined system. On the other hand, the strong fluid–wall interaction creates an LL layer on the wall. The thickness of the LL layer is small, within the range of 1–5σ, yielding sparsely distributed fluid particles in the bulk region of the channel, explaining the increased χ_{gas} in the confined system. Figure 13(a) shows that the equal-wall-temperature condition with $k_B T_{up}/\varepsilon = k_B T_{bot}/\varepsilon = 1.3302$ has a larger χ_{gas} than the

FIG. 13. The gas contents and vapor or liquid layer thicknesses in confined and unconfined systems. (a) χ dependent on β. (b) δ/H dependent on β.

non-equal-wall-temperature condition with $k_B T_{hot}/\varepsilon = 1.4542$ and $k_B T_{cold}/\varepsilon = 1.2062$. The heat transfer of fluid particles from the hot wall to the cold wall causes a non-uniform distribution of fluid particles across the channel height, lowering the χ_{gas} of the system.

Differences in fluid–wall interaction intensity strongly influence the organization of fluid particles near the walls. The vapor layer at a weak fluid–wall interaction and the liquid layer at a strong fluid–wall interaction represent two types of particle organizations near the walls, whose thicknesses are recorded as δ_{GL} and δ_{LL}, respectively. The red and black colors represent such definitions in Fig. 13(b), respectively. It is seen that for β values lower than 0.5 (corresponding to weak fluid–wall-interaction), a GL layer exists on the wall. Generally, the equal-wall-temperature cases yield a larger vapor layer thickness than the unequal-wall-temperature cases, which is thicker at the hot wall than at the cold wall. For β values larger than 0.6 (corresponding to strong fluid–wall-interaction), the cold wall maintains a thicker LL layer than the hot wall. The cold wall has a larger capability to adhere liquid particles, with a smaller distance between neighboring fluid particles.

Finally, we present an analogy for the phase distribution between subcritical and supercritical pressures. The left and right columns of Fig. 14 refer to phase distribution at subcritical and supercritical pressures, respectively. As is well documented in textbooks on multiphase flow, under conditions of a wetting surface and/or lower temperatures, a liquid layer attaches to the wall, and a gas phase is formed in the channel core. However, droplets may be entrained in the gas phase. The pattern shown in Fig. 14(a) is called an annular pattern, which exists widely in many heat exchanger tubes for adiabatic or heated multiphase flow,[43,57] in which the liquid film thickness dominates the heat transfer between wall and fluid. Here, we identify two patterns in Figs. 14(b) and 14(c) at a strong fluid–wall interaction, with $\beta > 0.6$ at supercritical pressure and an LL layer adhered to each of the two walls. The pattern either exhibits a three-layer structure for larger bulk fluid densities, or a five-layer structure for more moderate bulk fluid densities. The density profile in the channel is symmetrical for the equal-wall-temperature cases, but it is seriously deformed along the channel centerline for the equal-wall-temperature cases.

When using hydrophobic or superhydrophobic surfaces at subcritical pressures, a gas or vapor layer exists on the wall [see Fig. 14(d)], which is useful to reduce pressure drop for fluid transportation. Such a pattern is called the Lotus leaf effect.[43] Alternatively, when the wall temperature is sufficiently high (i.e., above a certain threshold), the liquid is completely vaporized to form a vapor layer on the wall to levitate droplets, which is called the Leidenfrost phenomenon.[58] Practically, a Leidenfrost pattern should be avoided owing to the weak heat transfer between wall and droplet. Figures 14(e) and 14(f) show the patterns at supercritical pressures. For weak fluid–wall interaction, a GL layer exists on each of the two walls. The pattern shows either a five-layer structure [see Fig. 14(e)] or a three-layer structure. It is interesting to note that the phase distributions shown in Fig. 14(e) and 14(f) are the inverse of those shown in Fig. 14(b) and 14(c), where the wall wettability (i.e., the fluid–wall interactions) reorganizes the fluid particles to yield the inverse pattern.

In this work, we simulated the nanochannel system using argon. It is found that at supercritical pressure, the fluid density is not only dependent on pressure and temperature, but also on the fluid–wall interactions, which is not supported by the classical thermodynamic
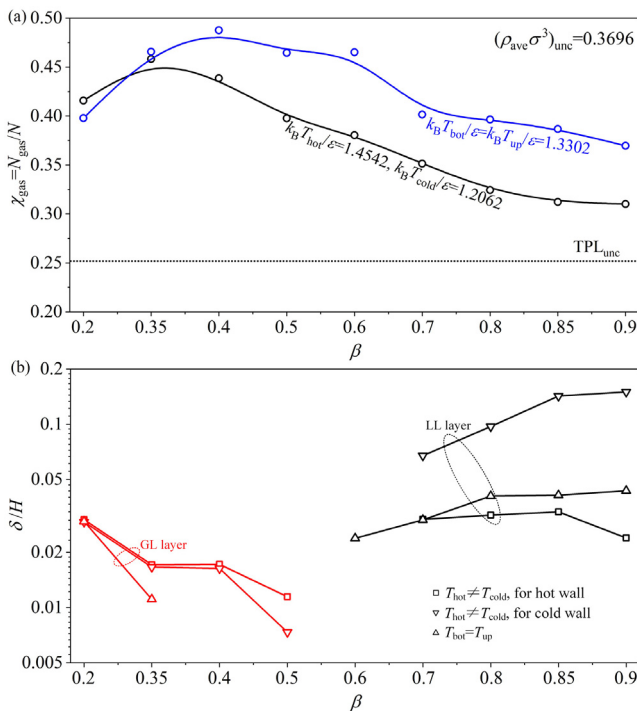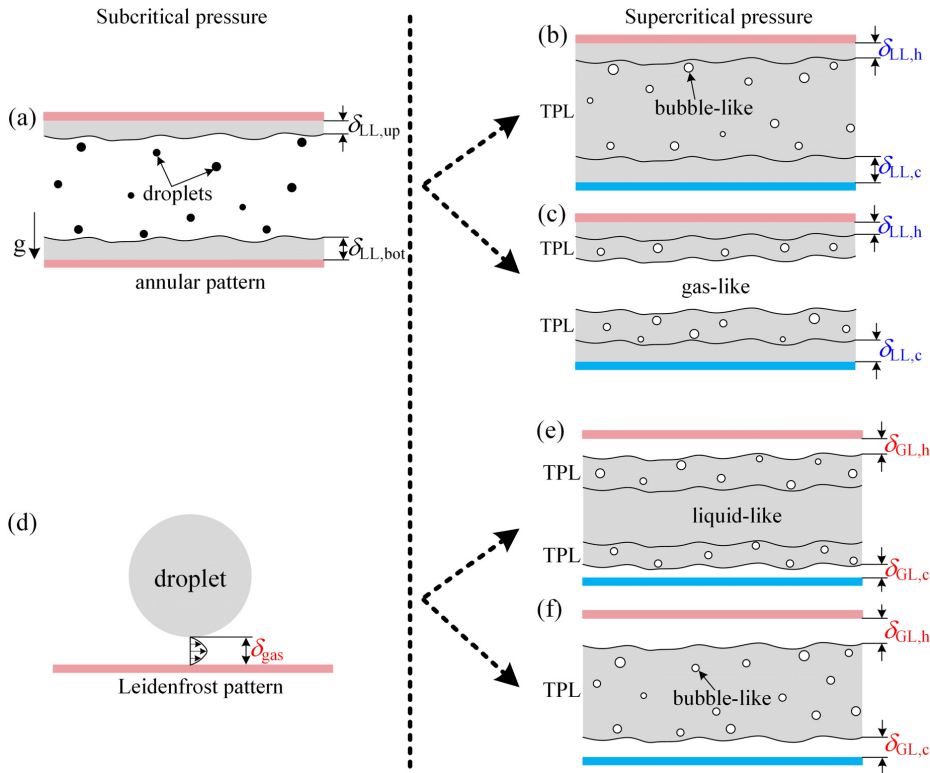
FIG. 14. The analogy of phase distribution in subcritical pressure and supercritical pressure. (a) Annular pattern with liquid-film on walls and two-phase structure containing droplets in subcritical pressure. (b) Three layer structure with LL layer on the wall and TPL in the channel core in supercritical pressure. (c) Five layer structure including two LL layers on the two walls, two TPL layers close to the LL payer, and a GL layer in the channel core in supercritical pressure. (d) Droplet floating on vapor layer (Leidenfrost pattern). (e) Five layer structure in supercritical pressure. (f) Three layers structure in supercritical pressure.

theory. Correspondingly, the phase pattern in nanochannels can be LL, GL, TPL, or a combination of these patterns. The top wall and the bottom wall have identical wettabilities. For identical temperatures of the top and bottom walls, fluid particles are symmetrically distributed in the channel without temperature gradient in the channel. When the temperatures are different for the two walls, heat transfer takes place across the two walls via the fluid particles. There is a strong connection between temperature gradient and phase distribution in the nanochannel. Clearly, temperature gradient is well established for heat transfer [see Fig. 15(a)]. Extending from the hot wall to the bulk fluid, fluid particles are sparsely distributed to display the TPL characteristics, which is the mixture of gas molecules and liquid molecules, except for a very thin LL layer on the hot wall. Near the cold wall, the liquid-like layer thickness is apparently larger than that at the hot wall [see Fig. 15(b)]. Figure 15 indicates that the phase distribution is not only dominated by the temperature gradient in the channel, but also influenced by the fluid–wall interactions.

It is known that at subcritical pressure, the distance between molecules is small for liquids, but becomes large for gas, and intermolecular forces determine the distance between fluid particles. Here, we identify that the state behavior in supercritical pressure is like that found at subcritical pressure, hence the LL, GL, and TPL can occur. The fluid–wall interactions influence the organization of fluid particles near the wall, and the effect of the fluid–wall-interactions can be extended to the bulk fluid. Temperature gradients in the nanochannel also influences the force interactions between fluid particles. Fluid particles at higher temperatures have high kinetic energy, hence fluid particles are sparsely populated. The temperature gradient in the

nanochannel causes the phase transition from one state to another state in the nanochannel (see Fig. 15).

Figure 16 further demonstrates that the phase distribution results from wall wettabilities and temperature gradient in the channel, noting
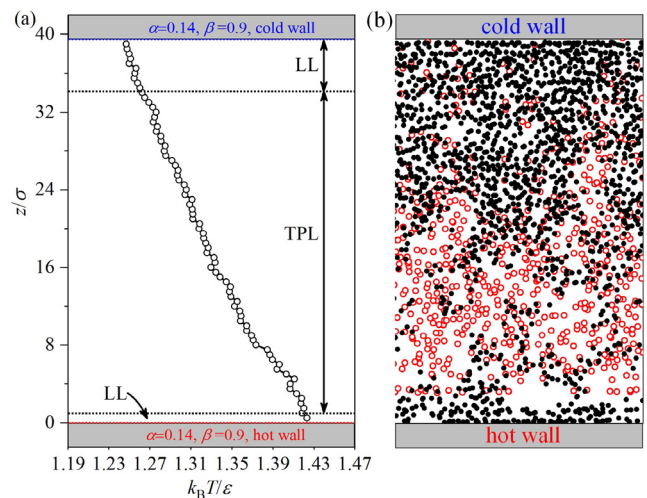

FIG. 15. The connection between the temperature gradient and the phase distribution in a nanochannel ($\beta_h = \beta_c = 0.9$, $k_B T_{hot}/\varepsilon = 1.4542$, $k_B T_{cold}/\varepsilon = 1.2062$, black and red colors represent the LL phase and GL phase, respectively). (a) Temperature profile in the nanochannel. (b) The distribution of fluid particles in the channel.
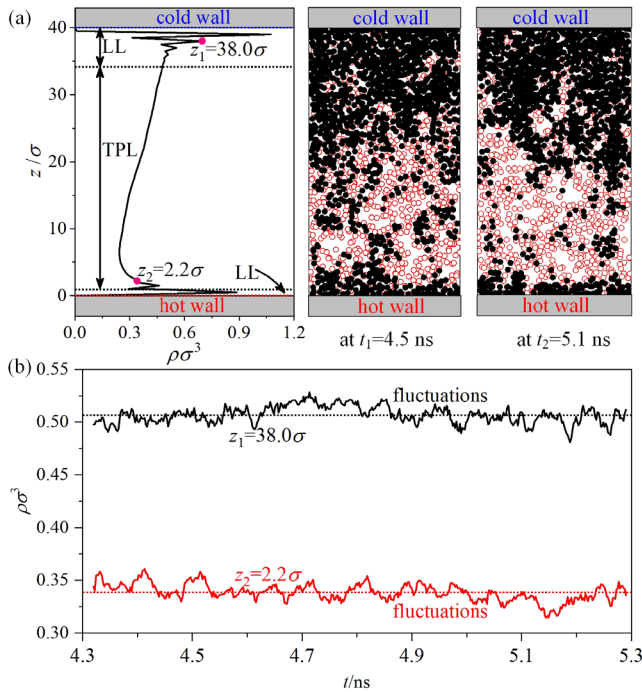
FIG. 16. The connection between the density distribution and the phase distribution in a nanochannel ($\beta_h = \beta_c = 0.9$, $k_B T_{hot}/\varepsilon = 1.4542$, $k_B T_{cold}/\varepsilon = 1.2062$, black and red colors represent the LL phase and GL phase, respectively). (a) Density profile in the nanochannel. (b) The distribution of fluid particles in the channel. (c) Fluctuations of densities at the two different locations.

identical computation condition for Figs. 15 and 16. Because the steady state problem is treated here, the phase distribution across the nanochannel is similar at 4.5 and 5.1 ns. Two locations are selected at $z_1 = 38.0\sigma$ and $z_2 = 2.2\sigma$, with LL at $z_1 = 38.0\sigma$, and TPL at $z_2 = 2.2\sigma$ [see Fig. 16(a)]. Figure 16(b) shows the fluid densities vs time at the two locations. Even though the densities are oscillating with mini amplitudes against their corresponding average values [see Fig. 16(b)], such fluctuations do not change the fluid state at the two locations. We recall that any parameter can be fluctuating with mini amplitudes. A small perturbation of the parameter would cause the change of the system state, which is an irreversible process.[59] The phenomenon observed in this paper is not caused by thermodynamic fluctuations.

The conclusions drawn in this paper are qualitatively suitable for other fluids such as water. Fundamentally, the phase distribution in nanochannels is influenced by fluid temperatures and the fluid–wall interactions. These two factors influence the force exerted on the fluid molecules to attract or separate the neighboring fluid molecules, thus affecting the density and phase distributions. This is true for both single atom molecules such as argon and other complex fluids such as water. The intermolecular force is the Van der Waals' force for argon, but includes the Van der Waals' force and the coulomb force for water. The phase distribution for water in supercritical state should be studied in the future.

IV. CONCLUSIONS

SFs are usually considered single-phase fluids without interfaces. Our recent investigations show that SFs contain complicated phase distributions, including nanobubble-like structures under unconfined conditions.[23] Inspired by this finding, we present the phase distributions for confined conditions, where the two walls confining the argon fluid have equal wettability but with equal or unequal wall temperatures. Our conclusions are summarized as follows:

1. This work indicates that fluid density is not only dependent on pressure and temperature but also on the fluid–wall interaction at confined conditions, deviating from the classical theory that at supercritical pressures, fluid density is dependent on pressure and temperature only.

2. For strong fluid–wall interactions, three- or five-layer structures are found that include LL layers on each of the two walls, and either TPL or GL layers (depending on bulk density) in the channel core. For weak fluid–wall interactions, the phase distribution becomes GL on the walls, and TPL and LL (depending on bulk density) in the channel core, which is opposite to that for strong fluid–wall interactions.

3. When using two walls with identical temperatures, the density profile in the channel is symmetrical along the channel centerline. However, when using different wall temperatures, symmetry-breaking may occur in the density and phase distribution along the channel centerline. The symmetry-breaking is obvious for strong fluid–wall interactions.

4. The LL or GL layer thickness dominates the flow and heat transfer for SFs in nanochannels. For strong fluid–wall interactions, the LL layer thickness is larger on the cold wall than on the hot wall. Alternatively, under weak fluid–wall interactions, the GL layer thickness is larger on the hot wall than on the cold wall.

5. A link is provided for the phase distribution at subcritical and supercritical pressures. For strong fluid–wall interactions with LL layers on the walls, the phase distribution is analogous to an annular pattern at subcritical pressures. For weak fluid–wall interactions with GL layers on the walls, the phase distribution is analogous to a Leidenfrost pattern at subcritical pressures.

AUTHOR DECLARATIONS
Conflict of Interest

The authors have no conflicts to disclose.

Author Contributions

Yan Wang: Writing – original draft (equal). **Jinliang Xu:** Writing – review & editing (equal). **Ming Dong:** Validation (equal). **Jian Xie:** Writing – review & editing (supporting). **Qinghua Wang:** Writing – review & editing (supporting).

DATA AVAILABILITY

The data that support the findings of this study are available from the corresponding author upon reasonable request.

07 December 2023 07:06:14

REFERENCES

[1]B. Berche, M. Henkel, and R. Kenna, "Fenômenos críticos: 150 anos desde Cagniard de la Tour," Rev. Bras. Ensino Fís. **31**, 2602.1 (2009).

[2]S. Lebonnois and G. Schubert, "The deep atmosphere of Venus and the possible role of density-driven separation of CO_2 and N_2," Nat. Geosci. **10**, 473–477 (2017).

[3]T. Kuritani, T. Yokoyama, and E. Nakamura, "Generation of rear-arc magmas induced by influx of slab-derived supercritical liquids: Implications from alkali basalt lavas from Rishiri Volcano, Kurile arc," J. Pet. **49**, 1319–1342 (2008).

[4]M. K. Hrnčič, D. Cör, M. T. Verboten et al., "Application of supercritical and subcritical fluids in food processing," Food Qual. Saf. **2**, 59–67 (2018).

[5]I. A. Makaryan, A. Y. Kostin, and I. V. Sedov, "Application of supercritical fluid technologies in chemical and petrochemical industries," Pet. Chem. **60**, 244–254 (2020).

[6]J. Xu, E. Sun, M. Li, H. Liu et al., "Key issues and solution strategies for supercritical carbon dioxide coal fired power plant," Energy **157**, 227–246 (2018).

[7]F. Crespi, G. Gavagnin, D. Sánchez et al., "Supercritical carbon dioxide cycles for power generation: A review," Appl. Energy **195**, 152–183 (2017).

[8]M. A. Boles and Y. A. Cengel, Thermodynamics: An Engineering Approach (McGraw-Hill, New York, 2011).

[9]G. G. Simeoni, T. Bryk, F. A. Gorelli et al., "The Widom line as the crossover between liquid-like and gas-like behaviour in supercritical fluids," Nat. Phys. **6**, 503–507 (2010).

[10]A. Idrissi, I. Vyalov, N. Georgi et al., "On the characterization of inhomogeneity of the density distribution in supercritical fluids via molecular dynamics simulation and data mining analysis," J. Phys. Chem. B **117**, 12184–12188 (2013).

[11]P. Gallo, D. Corradini, and M. Rovere, "Widom line and dynamical crossovers as routes to understand supercritical water," Nat. Commun. **5**, 5806 (2014).

[12]P. F. McMillan and H. E. Stanley, "Going supercritical," Nat. Phys. **6**, 479–480 (2010).

[13]D. Bolmatov, V. V. Brazhkin, Y. D. Fomin et al., "Evidence for structural crossover in the supercritical state," J. Chem. Phys. **139**, 234501 (2013).

[14]D. Bolmatov, D. Zav'yalov, M. Gao et al., "Structural evolution of supercritical CO_2 across the Frenkel line," J. Phys. Chem. Lett. **5**, 2785–2790 (2014).

[15]A. S. Raman, H. Li, and Y. C. Chiew, "Widom line, dynamical crossover, and percolation transition of supercritical oxygen via molecular dynamics simulations," J. Chem. Phys. **148**, 014502 (2018).

[16]A. Yamane, F. Shimojo, and K. Hoshino, "Effects of long-range interactions on the structure of supercritical fluid mercury: Large-scale molecular-dynamics simulations," J. Phys. Soc. Jpn. **75**, 124602 (2006).

[17]K. Ghosh and C. V. Krishnamurthy, "Structural behavior of supercritical fluids under confinement," Phys. Rev. E **97**, 012131 (2018).

[18]D. T. Banuti, "Crossing the Widom-line–supercritical pseudo-boiling," J. Supercrit. Fluids **98**, 12–16 (2015).

[19]F. Maxim, C. Contescu, P. Boillat et al., "Visualization of supercritical water pseudo-boiling at Widom line crossover," Nat. Commun. **10**, 4114 (2019).

[20]F. Maxim, K. Karalis, P. Boillat et al., "Thermodynamics and dynamics of supercritical water pseudo-boiling," Adv. Sci. **8**, 2002312 (2021).

[21]M. Y. Ha, T. J. Yoon, T. Tlusty et al., "Widom delta of supercritical gas–liquid coexistence," J. Phys. Chem. Lett. **9**, 1734–1738 (2018).

[22]M. Y. Ha, T. J. Yoon, T. Tlusty et al., "Universality, scaling, and collapse in supercritical fluids," J. Phys. Chem. Lett. **11**, 451–455 (2020).

[23]J. Xu, Y. Wang, and X. Ma, "Phase distribution including a bubblelike region in supercritical fluid," Phys. Rev. E **104**, 014142 (2021).

[24]U.S. Energy Information Administration (EIA), in International Energy Outlook 2017 (IEO2017) (EIA, 2017), p. 143.

[25]S. Wang, F. Javadpour, and Q. Feng, "Fast mass transport of oil and supercritical carbon dioxide through organic nanopores in shale," Fuel **181**, 741–758 (2016).

[26]C. Liu, Y. K. Shen, J. N. Zhang et al., "Production analysis in shale gas reservoirs based on fracturing-enhanced permeability areas," Sci. China Phys., Mech. Astron. **62**, 104611 (2019).

[27]E. Reverchon and R. Adami, "Nanomaterials and supercritical fluids," J. Supercrit. Fluids **37**, 1–22 (2006).

[28]L. Zhang, J. Xu, Q. Chen et al., "Switchable heat transfer in nano Janus-interface-system," Int. J. Heat Mass Transfer **127**, 761–771 (2018).

[29]T. Lin, J. Li, X. Quan et al., "A molecular dynamics investigation on effects of nanostructures on thermal conductance across a nanochannel," Int. Commun. Transfer **97**, 118–124 (2018).

[30]J. Vera and Y. Bayazitoglu, "Temperature and heat flux dependence of thermal resistance of water/metal nanoparticle interfaces at sub-boiling temperatures," Int. J. Heat Mass Transfer **86**, 433–442 (2015).

[31]M. Heier, F. Diewald, M. T. Horsch et al., "Molecular dynamics study of adsorption of the Lennard-Jones truncated and shifted fluid on planar walls," J. Chem. Eng. Data **64**, 386–394 (2019).

[32]Y. Li, M. Cui, B. Peng et al., "Adsorption behaviors of supercritical Lennard-Jones fluid in slit-like pores," J. Mol. Graph. Model. **83**, 84–91 (2018).

[33]F. Guo, S. Wang, Q. Feng et al., "Adsorption and absorption of supercritical methane within shale kerogen slit," J. Mol. Liq. **320**, 114364 (2020).

[34]S. Wang, Q. Feng, M. Zha et al., "Supercritical methane diffusion in shale nanopores: Effects of pressure, mineral types, and moisture content," Energy Fuels **32**, 169–180 (2018).

[35]R. F. Cracknell, D. Nicholson, and K. E. Gubbinst, "Molecular dynamics study of the self-diffusion of supercritical methane in slit-shaped graphitic micropores," J. Chem. Soc. Faraday Trans. **91**, 1377–1383 (1995).

[36]J. Zhou and W. Wang, "Adsorption and diffusion of supercritical carbon dioxide in slit pores," Langmuir **16**, 8063–8070 (2000).

[37]M. C. Gordillo and J. Mart, "Hydrogen bonding in supercritical water confined in carbon nanotubes," Chem. Phys. Lett. **341**, 250–254 (2001).

[38]B. Shan, R. Wang, Z. Guo et al., "Contribution quantification of nanoscale gas transport in shale based on strongly inhomogeneous kinetic model," Energy **228**, 120545 (2021).

[39]T. A. Ho, Y. Wang, A. Ilgen et al., "Supercritical CO_2-induced atomistic lubrication for water flow in a rough hydrophilic nanochannel," Nanoscale **10**, 19957–19963 (2018).

[40]S. Zhan, Y. Su, M. Lu et al., "Effect of surface type on the flow characteristics in shale nanopores," Geofluids **2021**, 6641922.

[41]Z. Yuan, H. Chen, and J. Zhang, "Facile method to prepare lotus-leaf-like super-hydrophobic poly(vinyl chloride) film," Appl. Surf. Sci. **254**, 1593–1598 (2008).

[42]L. Zhang, J. Xu, J. Lei et al., "The connection between wall wettability, boiling regime and symmetry breaking for nanoscale boiling," Int. J. Therm. Sci. **145**, 106033 (2019).

[43]V. P. Carey, Liquid-Vapor Phase-Change Phenomena: An Introduction to the Thermophysics of Vaporization and Condensation Processes in Heat Transfer Equipment (Taylor & Francis, Bristol, PA, 2020).

[44]L. Zhang and J. Xu, "Nucleate boiling of thin liquid films on nanostructured surfaces with hybrid wettability using molecular dynamics simulation," J. Mol. Liq. **366**, 120272 (2022).

[45]P. Yi, D. Poulikakos, J. Walther et al., "Molecular dynamics simulation of vaporization of an ultra-thin liquid argon layer on a surface," Int. J. Heat Mass Transfer **45**, 2087–2100 (2002).

[46]M. P. Allen and D. J. Tildesley, Computer Simulation of Liquids, 2nd ed. (Oxford University Press, 2017).

[47]J. E. Lennard-Jones, "Cohesion," Proc. Phys. Soc. **43**, 461 (1931).

[48]G. Nagayama, M. Kawagoe, A. Tokunaga et al., "On the evaporation rate of ultra-thin liquid film at the nanostructured surface: A molecular dynamics study," Int. J. Therm. Sci. **49**, 59–66 (2010).

[49]J. Delhommelle and P. Millié, "Inadequacy of the Lorentz-Berthelot combining rules for accurate predictions of equilibrium properties by molecular simulation," Mol. Phys. **99**, 619–625 (2001).

[50]G. Nagayama, T. Tsuruta, and P. Cheng, "Molecular dynamics simulation on bubble formation in a nanochannel," Int. J. Heat Mass Transfer **49**, 4437–4443 (2006).

[51]A. Shahmardi, O. Tammisola, M. Chinappi et al., "Effects of surface nanostructure and wettability on pool boiling: A molecular dynamics study," Int. J. Therm. Sci. **167**, 106980 (2021).

[52]T. Schneider and E. Stoll, "Molecular-dynamics study of a three-dimensional one-component model for distortive phase transitions," Phys. Rev. B **17**, 1302 (1978).

[53]S. Plimpton, "Fast parallel algorithms for short-range molecular dynamics," J. Comput. Phys. **117**, 1–19 (1995).

07 December 2023 07:06:14

[54]P. R. Ten Wolde and D. Frenkel, "Computer simulation study of gas–liquid nucleation in a Lennard-Jones system," J. Chem. Phys. **109**, 9901–9918 (1998).

[55]J. Losey and R. J. Sadus, "Structural behavior of fluids from the vapor and liquid region to the supercritical phase," Phys. Rev. E **100**, 052132 (2019).

[56]J. Wedekind and D. Reguera, "What is the best definition of a liquid cluster at the molecular scale?," J. Chem. Phys. **127**, 154516 (2007).

[57]C. D. Bowers and P. S. Hrnjak, "Developing two-phase R134a flow after an expansion valve in an 8.7 mm tube," in International Refrigeration And Air Conditioning Conference (2008).

[58]D. Quéré, "Leidenfrost dynamics," Annu. Rev. Fluid Mech. **45**, 197–215 (2013).

[59]D. C. Rapaport, *The Art of Molecular Dynamics Simulation* (Cambridge University Press, 2004).

07 December 2023 07:06:14